

Cite this: *Energy Adv.*, 2024,  
3, 307

# Decal Ni mesh to enhance the conductivity of carbon back contacts in dye sensitized and perovskite solar cells†

Jorge Martins,<sup>ab</sup> Marta Pereira,<sup>ab</sup> Seyedali Emami,<sup>ab</sup> Dzmitry Ivanou<sup>ab\*</sup> and Adélio Mendes<sup>ab\*</sup>

Dye-sensitized solar cells (DSSCs) and perovskite solar cells (PSCs) are photovoltaic (PV) technologies that originally utilized precious metals like gold, silver, and platinum as counter-electrodes. Carbon materials are a low-cost alternative to traditional metal counter-electrodes in monolithic-DSSCs (M-DSSCs) and PSCs. However, the drawback of carbon-based counter-electrodes is that they often show a low electronic conductivity, which hinders the scale-up of these PV technologies. This study proposes using decal Ni-mesh produced through simple and scalable photolithography-assisted electroplating. The Ni-mesh is incorporated into the carbon layer to improve the counter-electrode conductivity in large-area M-DSSCs and PSCs. Carbon-counter electrodes embedded with Ni-mesh enhance the performance of M-DSSCs and PSCs by 132% and 41%, respectively. Impedance spectroscopy study shows that the embedded Ni-mesh effectively reduces the series resistance of the devices by half, leading to an enhancement in their overall performance.

Received 26th September 2023,  
Accepted 10th December 2023

DOI: 10.1039/d3ya00476g

rsc.li/energy-advances

## 1. Introduction

Dye-sensitized solar cells (DSSCs) and perovskite solar cells (PSCs) are photovoltaic (PV) technologies with great potential for commercialization due to simple and versatile fabrication and good power conversion efficiency (PCE).<sup>1,2</sup> These devices possess good aesthetics, can be semitransparent, and display high power output under diffuse and artificial light.<sup>3</sup> Recent research has been focused on developing efficient semitransparent and bifacial devices,<sup>3,4</sup> using strategies such as tandem configuration,<sup>5,6</sup> and employing DSSCs and PSCs as indoor PVs for powering Internet-of-Things (IoT) low-power devices.<sup>7–9</sup> The prospect of reaching commercialization and the need of scaling up production from lab-scale to large-area devices raise awareness for sustainable materials and production methods.<sup>10,11</sup> One of the concerns is related to the counter-electrode; DSSCs and PSCs were initially developed with counter-electrodes made of noble metals such as gold, silver, and platinum due to the alignment of the electron work function, high conductivity, and

high catalytic activity (Pt).<sup>12,13</sup> These metals are expensive, and for application in PSCs, vacuum deposition methods are often used. Furthermore, they can present poor chemical stability in contact with some components of a cell (*e.g.*, Ag and Au corrosion in DSSC electrolyte) or can induce degradation in long-term device operation (*e.g.*, Au and Ag migration in PSCs).<sup>14–17</sup> Several carbon-based materials have emerged for the counter-electrode to provide a stable and cost-effective alternative.<sup>18,19</sup> Graphite,<sup>20,21</sup> carbon black (CB),<sup>22,23</sup> graphene,<sup>24,25</sup> carbon paper,<sup>26</sup> and carbon nanotubes (CNTs),<sup>27,28</sup> to name a few, have been studied as back contacts in DSSCs and PSCs. In particular, carbon black and graphite mixtures have been the reference carbon electrode for DSSCs and PSCs.<sup>20,29,30</sup>

Carbon materials are inexpensive and abundant, typically do not require sophisticated deposition techniques, and exhibit excellent chemical stability.<sup>31,32</sup> Nevertheless, the limitation in electrical conductivity of carbon electrodes is a significant concern.<sup>12,33,34</sup> This limitation becomes evident in the performance of large-area devices, where ohmic losses in both the carbon counter-electrode and the front-electrode, typically a transparent conductive oxide (TCO) layer, result in a substantial reduction in power conversion efficiency. In devices with an area of 36 cm<sup>2</sup>, the efficiency is reduced by an order of magnitude compared to laboratory-scale counterparts.<sup>35–37</sup> The low conductivity of carbon electrodes is a significant challenge when it comes to scaling up and manufacturing modules with high output power.

<sup>a</sup> LEPABE – Laboratory for Process, Environment, Biotechnology and Energy, Department of Chemical Engineering, Faculty of Engineering of University of Porto, Rua Dr. Roberto Frias s/n 4200-465, Porto, Portugal. E-mail: ivanou@fe.up.pt, mendes@fe.up.pt

<sup>b</sup> ALiCE – Associate Laboratory in Chemical Engineering, Faculty of Engineering of University of Porto, Rua Dr. Roberto Frias s/n 4200-465, Porto, Portugal

† Electronic supplementary information (ESI) available. See DOI: <https://doi.org/10.1039/d3ya00476g>



A simple and easy way to improve the conductivity of low-conductive materials is to use them with a metallic mesh.<sup>33,38,39</sup> Embedding a metallic mesh on TCO-coated glass substrates<sup>36,38–40</sup> and flexible electrodes<sup>41,42</sup> improves charge collection and leads to higher device performance.

Among various metals for preparing this conductive mesh, nickel emerges as a promising choice. It offers several advantages: it is more cost-effective and abundant than noble metals,<sup>14</sup> and its conductivity surpasses most carbon counter-electrodes. Nickel demonstrates chemical stability when exposed to iodide and cobalt-based electrolytes and is inert to perovskite precursors, while conventionally used metals like aluminum and copper tend to corrode.<sup>38,43</sup> Moreover, Ni-mesh preparation through electroplating is straightforward, removing the need for sophisticated and energy-intensive vacuum processes such as thermal evaporation or sputtering.<sup>42,44</sup>

In this study, a Ni-mesh was electrodeposited on fluorine-doped tin oxide (FTO)-coated glass, where the desired pattern of the mesh was created by photolithography. FTO-coated glasses were used as substrates because of their weak adhesion to the electrodeposited Ni;<sup>45</sup> the deposited mesh easily peels-off from the substrates. Photolithography-assisted electrodeposition allows whichever mesh design and easy application of the decal mesh to the carbon layers. The materials for this carbon-Ni composite counter-electrode are prepared individually and applied together during the fabrication of the devices. Composite carbon counter-electrodes are formulated by combining several materials before the fabrication process by dispersing other materials in a carbon matrix or integrating carbon-based materials in the matrix of other materials.<sup>46–48</sup>

The composite carbon-Ni significantly increased the charge collection, improving the fill factor and decreasing the ohmic losses in large-area DSSCs and PSCs. The PCE of large-area devices of 5 cm<sup>2</sup> was notably enhanced by 132% and 41% in a DSSC and a PSC, respectively, compared to conventional counterparts with unmodified carbon electrode layers.

## 2. Experimental

### 2.1 Fabrication of Ni mesh

Decal nickel mesh was prepared by photolithography-assisted electrochemical deposition. FTO-coated glasses (TEC-7; GreatCell Solar) served as substrates for Ni deposition; the photolithographically processed photoresist layer provided the desired pattern for the mesh. Fig. 1 sketches the steps of forming the nickel mesh. Briefly, the positive photoresist (AZ 4562; Microchemicals) was deposited onto FTO-glass substrates by spin coating (2000 rpm, 35 s) followed by soft-baking at 100 °C for 10 min (Fig. 1a). FTO glasses with a photoresist layer were exposed to UV light using an attached contrast black/white mask with a grid design (Fig. 1e). After UV exposure, the samples were treated in 1 : 4 (v/v) AZ 400 K (Microchemicals) developer diluted with water, opening in the photoresist layer the design of the desired mesh (Fig. 1b). The nickel was then electrodeposited using a simple setup with a two-electrode arrangement in a 250 ml glass beaker (Fig. 1c).



Fig. 1 Sketch of the Ni mesh fabrication process.

Watts electrolyte<sup>49</sup> was used for the nickel electrodeposition (pH 4, (50 ± 2) °C, stirring); the composition in g L<sup>-1</sup> of the electrolyte, after dilution in distilled water, was: NiSO<sub>4</sub>·6H<sub>2</sub>O (300), NiCl<sub>2</sub>·6H<sub>2</sub>O (35), and H<sub>3</sub>BO<sub>3</sub> (45). The FTO-coated glass/photoresist and the platinum counter-electrode mesh were inserted in the electrolyte solution, parallel and at a distance from each other of 5 cm. An electrochemical station (Autolab PGSTAT302N) was then used to drive a constant cathodic current of 36.5 mA cm<sup>-2</sup> for 10 min. The thickness of the deposited Ni layer estimated by SEM analysis (Fig. S1, ESI<sup>†</sup>) was (7.0 ± 0.1) μm.

### 2.2 Preparation of DSSCs

FTO-coated glass (2.2 mm, TEC7, GreatCell Solar) and bare soda-lime glass (3 mm, SGG PLANICLEAR, Saint-Gobain) were used as photoanode substrates and covers, respectively. A laser (355 nm nanosecond pulsed) was used to remove a section of the FTO layer (scribing) in the photoanode substrates and to drill the electrolyte injection holes in the cover glass. The substrates were ultrasonically washed with detergent and distilled water. After drying, the substrates were treated for 10 min in air plasma (Diener Electronics). A compact layer of TiO<sub>2</sub> was deposited on the photoanode substrates by spray pyrolysis at 450 °C, using a precursor solution of titanium diisopropoxide bis(acetylacetonate) in anhydrous 2-propanol, followed by a 45 min sintering step. Afterwards, a ca. 7 μm transparent mesoporous TiO<sub>2</sub> layer (Greatcell Solar 30 NR-D) was deposited and sintered at 500 °C for 1 h. DSSC devices of two sizes were prepared using square-shaped photoanodes: the smaller with a TiO<sub>2</sub> area of 0.25 cm<sup>2</sup> (denoted as S) and the larger with a TiO<sub>2</sub> area of 6.25 cm<sup>2</sup> (denoted as L). The substrates with the TiO<sub>2</sub> layer were treated with a 40 mM TiCl<sub>4</sub> aqueous solution at 70 °C for 30 min and sintered at 500 °C for 1 h. Afterward, a ca. 7 μm reflector/spacer TiO<sub>2</sub> layer (WER2-O, Greatcell Solar) and a carbon layer (Elcocarb B/SP, Solaronix) were sequentially deposited and sintered at 500 °C and 400 °C, respectively for 1 h. The thickness of the carbon layer was varied by depositing several carbon paste layers; SEM was used to determine the carbon layer thickness (Fig. S2, ESI<sup>†</sup>).



The substrates with the monolithic arrangement of DSSCs were immersed in a solution of 0.1 mM of the Y123 dye (Dyename) in *tert*-butanol/acetonitrile (1:1) %*(v/v)* for 48 h for the sensitization. Afterwards, the substrates were covered with bare glass and sealed with a 60  $\mu\text{m}$  thick thermoplastic sealant (Meltonix 1170-60, Solaronix) in a hotpress at 160  $^{\circ}\text{C}$ . The devices were filled with cobalt electrolyte containing 0.165 M of  $\text{Co}(\text{bpy})_3(\text{B}(\text{CN})_4)_2$  (Eversolar Co-200), 0.045 M of  $\text{Co}(\text{bpy})_3(\text{B}(\text{CN})_4)_3$  (Eversolar Co-300), 1.2 M *tert*-butyl pyridine (TBP) and 0.1 M  $\text{LiClO}_4$  (Sigma Aldrich) in acetonitrile. The injection holes were sealed with Surlyn<sup>®</sup> and a circular-shaped microscope glass slide.

### 2.3 Preparation of perovskite solar cells

The PSCs were prepared on FTO-glass substrates (2.2 mm, TEC7, GreatCell Solar). The substrates were scribed and washed, as described in Section 2.2. Then, a  $\text{TiO}_2$  compact layer was deposited using the same method as for DSSCs. Afterward, mesoporous layers of  $\text{TiO}_2$  (T165/SP, Solaronix),  $\text{ZrO}_2$  (ZT-SP, Solaronix), and carbon (Elcocarb B/SP, Solaronix) were deposited by screen printing. After deposition,  $\text{TiO}_2$  and  $\text{ZrO}_2$  layers were sintered at 500  $^{\circ}\text{C}$  for 1 h and the carbon layer at 400  $^{\circ}\text{C}$  for 1 h. The perovskite precursor consisting of  $(5\text{-AVA})_{0.05}(\text{MA})_{0.95}\text{PbI}_3$  in  $\gamma$ -butyrolactone (GBL) solution (Solaronix) was dropped on top of the mesoporous layers and crystallized at 70  $^{\circ}\text{C}$  for 30 min in a hot plate.

### 2.4 Application of the Ni mesh in/on the carbon counter-electrode

**DSSCs.** Two approaches were used to apply the metal mesh in DSSCs: (i) embedded in the carbon layer and (ii) atop the carbon layer (Fig. S3, ESI<sup>†</sup>). In the first approach, a carbon layer was screen-printed, followed by the Ni-mesh applied over the wet carbon, and dried at 120  $^{\circ}\text{C}$  for 15 min. Then, another carbon layer was screen-printed atop and sintered at 400  $^{\circ}\text{C}$  for 1 h; nickel mesh was sandwiched between the carbon layers. In the second approach, the metallic mesh was applied atop the carbon layer after the sensitization step. The Ni-mesh was mechanically pressed onto the device by the cover glass to achieve electrical contact. Fig. 2 shows a large-area DSSC device with the Ni-mesh.

**PSCs.** The preparation steps of the PSCs with incorporated Ni mesh are sketched in Fig. S4 (ESI<sup>†</sup>). The mesh was applied

atop the perovskite infiltrated mesoporous layers, and then low sintering temperature carbon paste (DN-CP01, Dyename) was deposited on top of the Ni mesh by screen printing; the carbon paste was dried at 100  $^{\circ}\text{C}$  for 15 min.

### 2.5 Characterization

The photocurrent–potential (*J*–*V*) curves were obtained under simulated solar light AM 1.5G, 100  $\text{mW cm}^{-2}$  from an Oriel class ABA LED solar simulator (MiniSol LSH 732; Newport). An electrochemical workstation (Zahner; Zennium) was employed to record the current *vs.* potential curves at 50  $\text{mV s}^{-1}$  and 10  $\text{mV s}^{-1}$  for DSSCs and PSCs, respectively. The PV devices were measured with a mask of 0.16  $\text{cm}^2$  (small devices) and 5.29  $\text{cm}^2$  (large devices). A batch of 4 devices was used for each test condition. The average values and the standard deviation for each batch are indicated in the tables. Characteristic *J*–*V* curves are presented for the device with the closest performance to the average value in a batch. Scanning electron microscopy (SEM) was characterized using a desktop SEM Phenom XL. The sheet resistance was measured using the Van der Pauw method with a Keithley 2425-C SourceMeter. The electrochemical impedance spectra (EIS) were collected in the dark in the frequency range of 1 MHz–0.1 Hz applying a sinusoidal perturbation with an amplitude of 10 mV at  $-0.85$  V (DSSCs) and  $-0.80$  V (PSCs). The EIS spectra were analyzed and fitted in ZView<sup>®</sup> software.

## 3. Results and discussion

### 3.1 Characterization and effect of carbon counter-electrode thickness on the performance of the PV devices

**DSSCs.** The reference carbon counter-electrode used in monolithic DSSCs (M-DSSCs) and hole conductor-free PSCs (HTM-free PSCs) is formed by a carbon black and graphite mixture applied by screen-printing. The carbon-electrode presents high electric resistivities between 5  $\Omega \text{sq}^{-1}$  and 12  $\Omega \text{sq}^{-1}$  (Fig. 3a and Table S1, ESI<sup>†</sup>), similar to the resistivity of the FTO-layer front contact, which usually ranges from 5  $\Omega \text{sq}^{-1}$  to 15  $\Omega \text{sq}^{-1}$ .<sup>50–54</sup>

A simple approach to improve the carbon-counter electrode conductivity is to increase its thickness (Fig. 3a). However, this approach has limited applicability since thick counter-electrodes can hinder the performance of devices, even in small-area devices, as indicated by the photovoltaic response (Fig. 3b) and metrics (Table S2, ESI<sup>†</sup>) of DSSCs with different carbon layer thicknesses.

The devices with 13  $\mu\text{m}$  and 32  $\mu\text{m}$  carbon films show similar photovoltaic responses with a power conversion efficiency (PCE) of *ca.* 7.3%. The cells generate an open-circuit potential ( $V_{\text{oc}}$ ) of *ca.* 0.87 V, a short circuit current density ( $J_{\text{sc}}$ ) of *ca.* 11.2  $\text{mA cm}^{-2}$ , and a fill factor ( $\eta_{\text{FF}}$ ) of *ca.* 0.77. The devices with a thicker 44  $\mu\text{m}$  carbon layer displayed a much lower PCE of 4.5% due to a noticeably low  $J_{\text{sc}}$  of 7.0  $\text{mA cm}^{-2}$ . The low performance of devices with a thick carbon layer was assigned to the deficient sensitization of the mesoporous  $\text{TiO}_2$  layer; the photoanodes are unevenly stained and have areas with poor dye loading – Fig. S5 (ESI<sup>†</sup>). The thick carbon layer



Fig. 2 Photograph of a large-area DSSC with applied Ni-mesh on the carbon-counter electrode; view from the side of the cover glass (a) and FTO-glass (b).





Fig. 3 Measured  $R_{\text{sheet}}$  vs. thickness of screen-printed carbon layers (a), and  $J$ - $V$  curves of small area (S) DSSCs with carbon counter electrodes of different thicknesses (b).

hinders the dye infiltration to the  $\text{TiO}_2$  layer, leading to deficient sensitization and underperforming devices.

**PSCs.** The photovoltaic response of HTM-free PSCs with different carbon electrode thicknesses has already been studied.<sup>22</sup> Most studies conclude that HTM-free PSCs display the highest PCE with an optimum carbon layer thickness in the range of 10 to 15  $\mu\text{m}$ ;<sup>55–63</sup> in the present study, the thickness of the carbon layer was chosen to be 13  $\mu\text{m}$ .

### 3.2 Large-area PV devices with embedded Ni mesh

**DSSCs.** The Ni-mesh was applied to large-area DSSCs (L) with carbon layers of 13  $\mu\text{m}$  and 32  $\mu\text{m}$ . The  $J$ - $V$  curves of the cells are plotted in Fig. 4 and Table 1 summarizes their photovoltaic metrics. Devices with pristine carbon electrodes have a low fill factor due to the ohmic losses at the carbon-counter electrode and at the FTO layer in the front electrode.<sup>36</sup> The DSSCs with 13  $\mu\text{m}$  and 32  $\mu\text{m}$  carbon layers delivered PCEs of 1.9% and 2.9%, respectively. The higher PCE is related to the higher photocurrent. Nevertheless, the  $J$ - $V$  response of both devices is a straight line, which indicates that high series resistances are hindering the photocurrent response.

Implementing the Ni-mesh on the counter-electrodes improves the performance of the devices, enhancing the photocurrent and

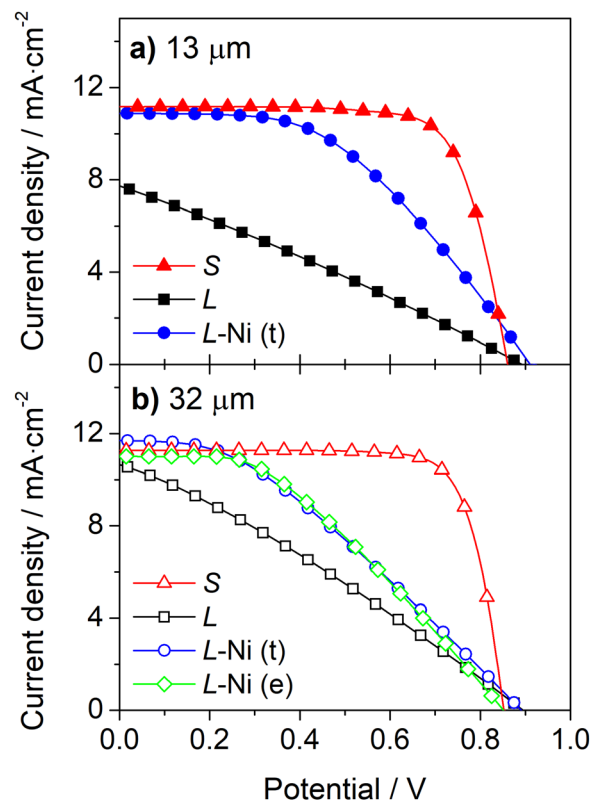


Fig. 4  $J$ - $V$  curves of large-area DSSCs (L) with 13  $\mu\text{m}$  (a) and 32  $\mu\text{m}$  (b) carbon layers without and with Ni-mesh applied on top (t) or embedded (e) in the carbon layer; curves (S) represent the photovoltaic response of devices with a small area photoanode.

the fill factor (Fig. 4 and Table 1). When Ni-mesh is applied on top of the 13  $\mu\text{m}$  thick carbon layer, the  $\eta_{\text{FF}}$  and  $J_{\text{sc}}$  rise from 0.28 and 7.5  $\text{mA cm}^{-2}$  to 0.46 and 10.7  $\text{mA cm}^{-2}$ , respectively; the PCE increased from 1.9% to 4.4%, translating to an impressive 132% improvement.

In the devices with a 32  $\mu\text{m}$  carbon layer, the Ni-mesh was applied on top (t) or embedded (e) in the carbon layer. In both cases, the metallic mesh improved the photovoltaic response. The PCE of the cells was increased from 2.9% to 3.7% (t) and 3.8% (e). Applying the metallic mesh on the top of the carbon layer (L-Ni(t)) increased the fill factor by 20%; the  $J_{\text{sc}}$  had a minor improvement of 5%, and the  $V_{\text{oc}}$  did not vary. When the mesh was embedded in the carbon layer (L-Ni(e)), the fill factor increased by 37%, while the  $J_{\text{sc}}$  and  $V_{\text{oc}}$  decreased slightly by 3.7% and 3.3%, respectively. Overall, Ni-mesh, either on top or embedded in the carbon layer, improved the performance of DSSCs by *ca.* 29%.

The internal resistances were obtained by EIS analysis for the devices with and without the Ni-mesh on the counter-electrode. The Nyquist plots of the L, L-Ni, and S devices are shown in Fig. 5. The series resistance ( $R_{\text{s}}$ ), charge transfer resistance at the counter electrode ( $R_{\text{CE}}$ ), and the electron recombination resistance at the photoanode ( $R_{\text{k}}$ ) were obtained by fitting the spectra to the equivalent circuit model (Fig. 5c) to the EIS data and are presented in Table 2.  $Q_{\text{CPE-CE}}$  and



**Table 1** Average and standard deviation photovoltaic metrics of large-area DSSCs (L) with 13  $\mu\text{m}$  and 32  $\mu\text{m}$  carbon films without and with Ni-mesh and small-area device (S) metrics

| Carbon thickness/ $\mu\text{m}$ | Device  | $V_{oc}/\text{V}$ | $J_{sc}/\text{mA cm}^{-2}$ | $\eta_{FF}$     | PCE/%         |
|---------------------------------|---------|-------------------|----------------------------|-----------------|---------------|
| 13                              | S       | $0.86 \pm 0.01$   | $11.1 \pm 0.1$             | $0.75 \pm 0.01$ | $7.2 \pm 0.1$ |
|                                 | L       | $0.89 \pm 0.00$   | $7.5 \pm 0.2$              | $0.28 \pm 0.00$ | $1.9 \pm 0.1$ |
|                                 | L-Ni(t) | $0.90 \pm 0.01$   | $10.7 \pm 0.6$             | $0.46 \pm 0.05$ | $4.4 \pm 0.2$ |
| 32                              | S       | $0.88 \pm 0.00$   | $11.3 \pm 0.2$             | $0.78 \pm 0.00$ | $7.4 \pm 0.1$ |
|                                 | L       | $0.90 \pm 0.01$   | $10.8 \pm 0.2$             | $0.30 \pm 0.01$ | $2.9 \pm 0.1$ |
|                                 | L-Ni(t) | $0.90 \pm 0.01$   | $11.3 \pm 0.5$             | $0.36 \pm 0.01$ | $3.7 \pm 0.2$ |
|                                 | L-Ni(e) | $0.87 \pm 0.02$   | $10.4 \pm 0.6$             | $0.41 \pm 0.01$ | $3.8 \pm 0.0$ |

$Q_{CPE_k}$  are constant phase elements associated with the counter-electrode/electrolyte and photoanode/electrolyte interfaces, respectively.

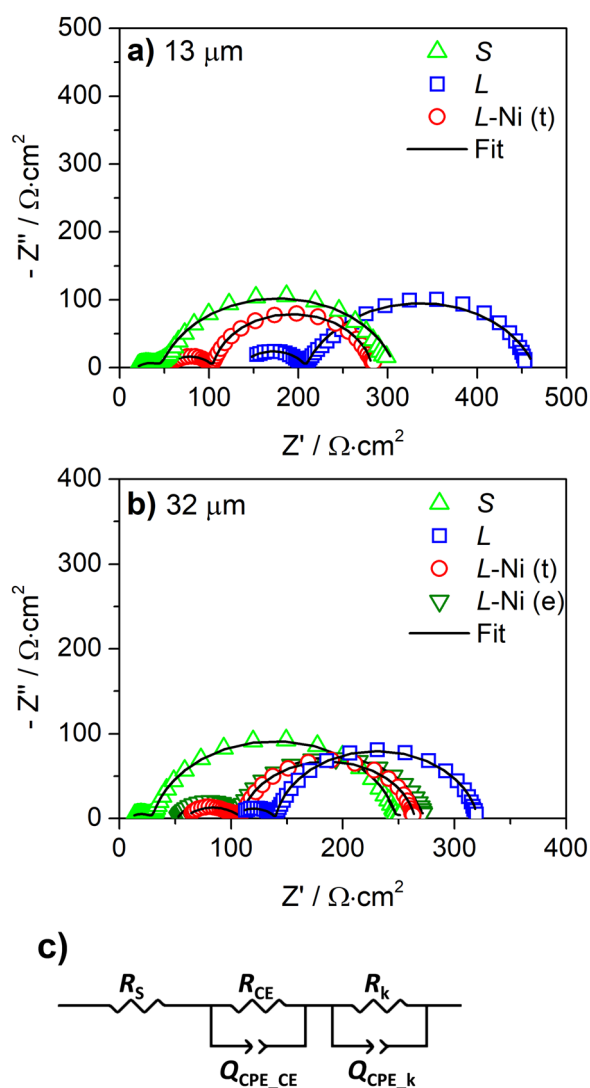


**Fig. 5** Nyquist diagrams of DSSCs with 13  $\mu\text{m}$  (a) and 32  $\mu\text{m}$  (b) carbon layer back contacts, for (S) small area devices, (L) large area devices without Ni-mesh applied, (L-Ni(t)) large area devices with Ni-mesh applied on top, and (L-Ni(e)) large area devices with Ni-mesh embedded in the counter-electrode layer; (c) equivalent circuit model used to fit the spectra.

The small area devices show a lower  $R_s$  value when the carbon counter-electrode is thicker; this correlates with the sheet resistance of the carbon layers previously presented (Fig. 3a and Table S1, ESI†).  $R_s$  decreased from 17.0 to 8.4  $\Omega \text{ cm}^2$  (Table 2) when the carbon counter-electrode thickness increased from 13  $\mu\text{m}$  to 32  $\mu\text{m}$ , and the sheet resistance of the carbon layers decreased from 11.5 to 6.0  $\Omega \text{ sq}^{-1}$  for 13  $\mu\text{m}$  and 32  $\mu\text{m}$  layers, respectively (Table S1, ESI†).

Large-area devices without Ni-mesh show high  $R_s$  values, above 100  $\Omega \text{ cm}^2$  (Table 2); the photovoltaic performance of L-cells is then greatly affected by the ohmic losses of the carbon-counter electrode. The poor conductivity of the carbon layer reduces the charge collection at the counter-electrode and limits the charge transfer process at the counter-electrode/electrolyte interface. L-cells with 13  $\mu\text{m}$  and 32  $\mu\text{m}$  carbon layers display an  $R_{CE}$  of 100  $\Omega \text{ cm}^2$  and 40  $\Omega \text{ cm}^2$ , respectively, considerably higher than for the small devices (S) with an  $R_{CE}$  of only 20  $\Omega \text{ cm}^2$ . The higher  $R_{CE}$  and  $R_s$  of the L devices with a 13  $\mu\text{m}$  counter-electrode determined the inferior device performance compared with cells with a 32  $\mu\text{m}$  carbon layer (Table 1). A minor difference in photovoltaic response was observed in small-area DSSCs with 13  $\mu\text{m}$  and 32  $\mu\text{m}$  carbon layers. These results confirm that the conductivity of the carbon layer is only relevant for the large-area cells.

The application of the Ni-mesh reduced the  $R_s$  of the L devices from above 100  $\Omega \text{ cm}^2$  to ca. 53  $\Omega \text{ cm}^2$ . However, the  $R_s$  values are still higher compared to those of the small cells ( $< 17 \Omega \text{ cm}^2$ ). The reason for that is the resistance of the FTO-coated glass when the device is scaled up.<sup>28</sup> The prepared large-area cells with an embedded Ni-mesh at the counter-electrode display similar  $R_{CE}$  values 37–39  $\Omega \text{ cm}^2$ . This shows that when used together with the

**Table 2** Resistances of the devices obtained by fitting the equivalent circuit model (Fig. 5c) to the Nyquist diagrams

| Carbon thickness/ $\mu\text{m}$ | Device  | $R_s/\Omega \text{ cm}^2$ | $R_{CE}/\Omega \text{ cm}^2$ | $R_k/\Omega \text{ cm}^2$ |
|---------------------------------|---------|---------------------------|------------------------------|---------------------------|
| 13                              | S       | 17.0                      | 22.2                         | 245.6                     |
|                                 | L       | 120.6                     | 98.8                         | 251.2                     |
|                                 | L-Ni(t) | 54.7                      | 38.9                         | 172.3                     |
| 32                              | S       | 8.4                       | 17.4                         | 201.2                     |
|                                 | L       | 100.5                     | 39.8                         | 180.6                     |
|                                 | L-Ni(t) | 53.9                      | 37.9                         | 137.3                     |
|                                 | L-Ni(e) | 52.1                      | 37.2                         | 119.4                     |



metallic mesh, the thickness of the carbon layer has no effect on the charge transfer process at the counter electrode/electrolyte interface.

The conductivity of the counter-electrode is one of the decisive factors for obtaining high photocurrents and fill factors; it becomes especially critical for high irradiances (Fig. 6 and 7). Fig. 6 and Table S3 (ESI†) show the  $J$ - $V$  curves and photovoltaic parameters of a DSSC device incorporating a 13  $\mu\text{m}$  carbon layer counter-electrode with an embedded Ni-mesh for light irradiances ranging from 0.1 up to 2 suns; for this device, the current density continuously increases with the light irradiance. On the other hand, the photocurrent of a cell incorporating a simple 13  $\mu\text{m}$  carbon layer counter-electrode (Fig. 6a) is similar for light irradiances above 1 sun since the conductivity of the counter-electrode limits the photogenerated current. Applying the Ni-mesh considerably increases the photocurrent at light irradiances above 1 sun (Fig. 6b). Moreover, the devices with Ni-mesh show higher  $\eta_{\text{FF}}$  for all light irradiances due to the improved conductivity of the counter-electrode.

Similar to the devices incorporating a 13  $\mu\text{m}$  carbon layer, embedding a Ni-mesh in a 32  $\mu\text{m}$  carbon layer improves the  $\eta_{\text{FF}}$  of the devices at all light intensities (Fig. 7 and Table S4, ESI†), and its effect on the photocurrent of devices increases with the light intensity (Fig. 7b and c).

Even the current density of the large DSSC device, incorporating a counter-electrode thickness of 32  $\mu\text{m}$ , is hindered by the ohmic losses at the carbon layer for light irradiances above 1

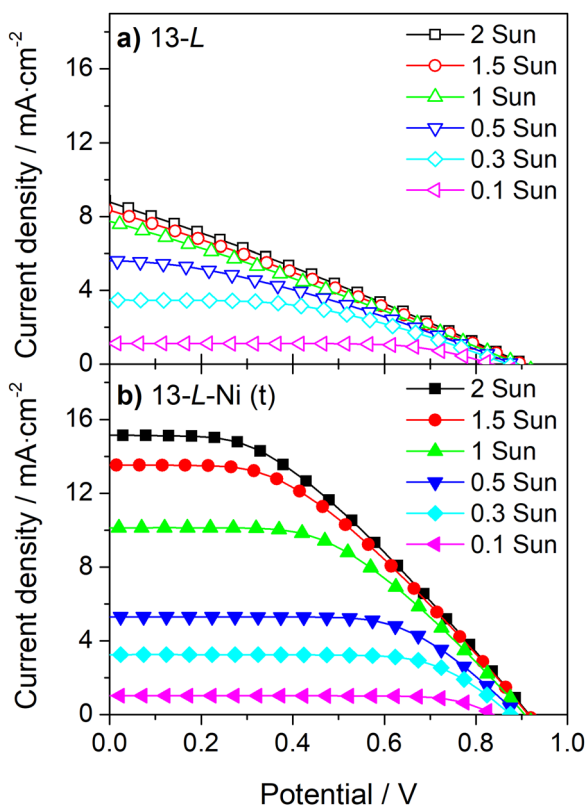


Fig. 6 Incident light-dependent current-density vs. potential curves of large-area DSSCs with 13  $\mu\text{m}$  carbon film (13-L) without (a) and with (b) Ni-mesh applied on top (t) of the carbon layer.

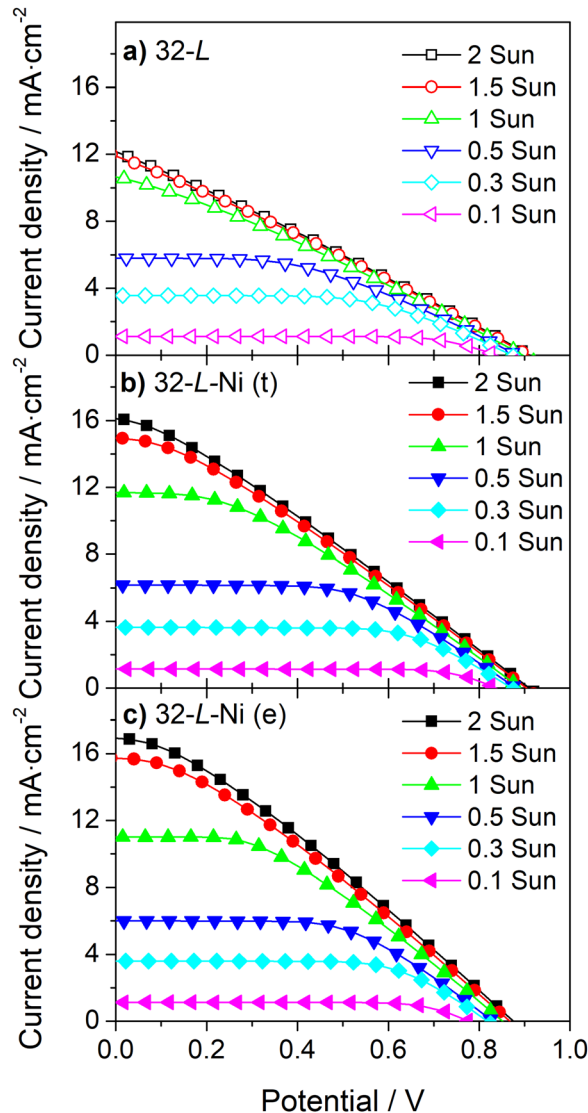


Fig. 7  $J$ - $V$  curves at different incident light intensities for large-area DSSCs with 32  $\mu\text{m}$  carbon film without (a) and with Ni-mesh applied on top (b) or embedded in the carbon layer (c).

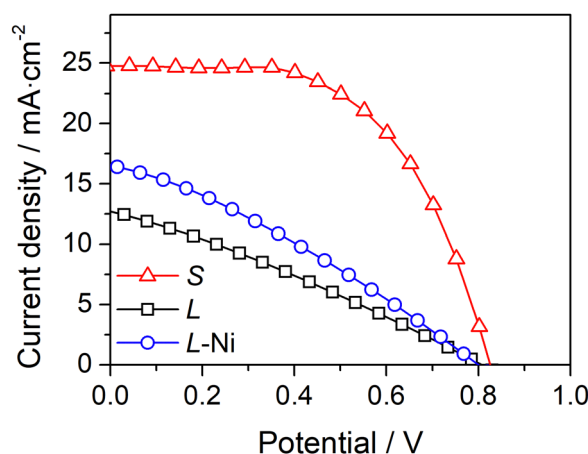


Fig. 8  $J$ - $V$  curves of large-area PSCs (L) without and with Ni mesh along the small area device (S).



**Table 3** Average and standard deviation photovoltaic parameters of large-area PSCs (L) without and with Ni mesh along small-area devices (S)

| Device | $V_{oc}/V$      | $J_{sc}/\text{mA cm}^{-2}$ | $\eta_{FF}/\%$  | PCE/%          |
|--------|-----------------|----------------------------|-----------------|----------------|
| S      | $0.82 \pm 0.01$ | $24.8 \pm 0.3$             | $0.58 \pm 0.01$ | $11.9 \pm 0.5$ |
| L      | $0.83 \pm 0.01$ | $12.9 \pm 1.1$             | $0.27 \pm 0.00$ | $2.9 \pm 0.3$  |
| L-Ni   | $0.81 \pm 0.01$ | $16.3 \pm 0.5$             | $0.31 \pm 0.02$ | $4.1 \pm 0.4$  |

sun (Fig. 7a). This fact highlights that strategies for improving carbon-counter electrode conductivity are relevant and necessary for developing high-power output commercial devices.

**PSCs.** Similar to DSSCs, the low conductivity of the carbon back contact negatively affects the performance of large-area PSCs, since they rely on this carbon layer for charge collection. The characteristic  $J$ - $V$  curves and photovoltaic parameters of large HTM-free PSCs without and with a Ni-mesh are presented in Fig. 8 and Table 3. Embedding the Ni-mesh on the carbon layer increases the  $J_{sc}$  and  $\eta_{FF}$  of the large area PSCs by ca. 26% and 15%, respectively. The Ni-mesh enhances the performance of the cells by 41%, improving the PCE from 2.9% to 4.1%. The PCE increases because the series resistance decreases (Fig. S6 and Table S5, ESI†).

The application of a Ni-mesh reduced the  $R_s$  of large-area devices from  $73.5 \Omega \text{ cm}^2$  to  $36.5 \Omega \text{ cm}^2$ . Small area devices (S) show  $R_s$  values of  $18.9 \Omega \text{ cm}^2$ , inferior to the L cells and similar to the DSSCs with the same carbon layer thickness. The higher  $R_s$  of large area PSCs with embedded Ni-mesh, compared to the small cells, implies that the photovoltaic performance of the devices is limited by the ohmic losses at the carbon layer but also at the TCO layer. Several strategies to improve the TCO layer conductivity are proposed in the literature<sup>39,40</sup> and can be implemented and assessed in further research in combination with the Ni-mesh in the back-contact.

## 4. Conclusions

The poor conductivity of carbon-counter electrodes is a major obstacle to obtaining efficient scaled-up M-DSSCs and PSCs. Improving the conductivity of carbon electrodes by just increasing the carbon layer thickness has relevant drawbacks, namely related to the sensitization of the photoanode with the dye, in the case of the DSSC devices, and the perovskite absorber infiltration and crystallization, in the case of PSCs.

This work addresses the low electric conduction of the carbon-based counter-electrodes by incorporating decal Ni-mesh on the carbon layer. The decal Ni-mesh was prepared by Ni electroplating on FTO-coated glasses; and photolithography was used to create the desired mesh pattern. The performance of the large-area M-DSSCs with  $13 \mu\text{m}$  and  $32 \mu\text{m}$  carbon layers and embedded Ni-mesh improved from 1.9% and 2.9% to 4.4% and 3.8%, respectively, mainly due to an improved  $\eta_{FF}$  and  $J_{sc}$ , showing that the best-performing counter-electrode was made of a  $13 \mu\text{m}$  carbon layer with an embedded Ni-mesh. Moreover, for high incident light irradiances above 1 sun, the DSSC devices with a simple carbon layer as a counter-electrode showed a saturated current density. However, when a Ni-mesh was

incorporated, the current density considerably increased with the irradiance above 1 sun.

An equivalent behavior was observed for the PSCs. When the Ni-mesh was applied to a large-area PSC, the power conversion efficiency increased from 2.9% to 4.1%. The improved performance when incorporating the Ni-mesh was assigned to a reduction to half of the series resistance, which decreased the ohmic losses of the carbon-based counter-electrode.

Electroplating Ni is a simple, low cost and widely used industrial process for various applications. The fabrication of the Ni-mesh by this method and the integration of a composite carbon-Ni counter-electrode into DSSC and PSC devices is advantageous for the upscaling of these technologies. A stand-alone Ni-mesh can easily be produced in different shapes and sizes and incorporated into other materials to improve their conductivity.

## Conflicts of interest

The authors declare that they have no known competing financial interests or personal relationships that could have appeared to influence the work reported in this paper.

## Acknowledgements

Jorge Martins and Marta Pereira are grateful to the Portuguese Foundation for Science and Technology (FCT) for their PhD grant (references SFRH/BD/147201/2019 and 2021.06451.BD, respectively). This work was financially supported by: (i) LA/P/0045/2020 (ALiCE), UIDB/00511/2020, and UIDP/00511/2020 (LEPABE), funded by national funds through FCT/MCTES (PIDDAC); (ii) project 2SMART (NORTE-01-0145-FEDER-000054), supported by Norte Portugal Regional Operational Programme (NORTE 2020), under the PORTUGAL 2020 Partnership Agreement, through the European Regional Development Fund (ERDF); (iii) project TanPT (2022.05826.PTDC), funded by FEDER funds through COMPETE2020 – Programa Operacional Competitividade e Internacionalização (POCI) and by national funds (PIDDAC) through FCT/MCTES; (iv) project Diamond funded by the European Union's Horizon Europe Framework Programme for research and innovation Programme under the grant agreement no. 101084124; (v) alliance for energy transition (ATE) no. C644914747-00000023, project 56 of the Incentive System “Agendas for Business Innovation”, financed by the Recovery and Resilience Plan (PRR) and by European Funds NextGeneration EU.

## References

- M. Kokkonen, P. Talebi, J. Zhou, S. Asgari, S. A. Soomro, F. Elsehrawy, J. Halme, S. Ahmad, A. Hagfeldt and S. G. Hashmi, *J. Mater. Chem. A*, 2021, **9**, 10527–10545.
- M.-J. Wu, C.-C. Kuo, L.-S. Jhuang, P.-H. Chen, Y.-F. Lai and F.-C. Chen, *Adv. Energy Mater.*, 2019, **9**, 1901863.
- X. Xie, Y. Zhang, Y. Ren, L. He, Y. Yuan, J. Zhang and P. Wang, *J. Phys. Chem. C*, 2022, **126**, 11007–11015.



- 4 C. Hora, F. Santos, M. G. F. Sales, D. Ivanou and A. M. Mendes, *ACS Appl. Energy Mater.*, 2022, **5**, 14846–14857.
- 5 L. Yuan, H. Michaels, R. Roy, M. Johansson, V. Öberg, A. Andruszkiewicz, X. Zhang, M. Freitag and E. M. J. Johansson, *ACS Appl. Energy Mater.*, 2020, **3**, 3157–3161.
- 6 G. Gianola, R. Speranza, F. Bella and A. Lamberti, *Sol. Energy*, 2023, **265**, 112116.
- 7 S. Venkatesan, T.-H. Hsu, H. Teng and Y.-L. Lee, *Solar RRL*, 2023, **7**, 2300220.
- 8 C. Teixeira, P. Spinelli, L. A. Castriotta, D. Müller, S. Öz, L. Andrade, A. Mendes, A. D. Carlo, U. Würfel, K. Wojciechowski and D. Forgács, *Adv. Funct. Mater.*, 2022, **32**, 2206761.
- 9 S. Mishra, S. Ghosh, B. Boro, D. Kumar, S. Porwal, M. Paul, H. Dixit and T. Singh, *Energy Adv.*, 2022, **1**, 761–792.
- 10 G. Spinelli, M. Freitag and I. Benesperi, *Sustainable Energy Fuels*, 2023, **7**, 916–927.
- 11 A. Alberti, E. Smecca, S. Valastro, I. Deretzis, G. Mannino, C. Bongiorno, G. Fiscaro and A. La Magna, *Phys. Chem. Chem. Phys.*, 2022, **24**, 21549–21566.
- 12 A. B. Muñoz-García, I. Benesperi, G. Boschloo, J. J. Concepcion, J. H. Delcamp, E. A. Gibson, G. J. Meyer, M. Pavone, H. Pettersson, A. Hagfeldt and M. Freitag, *Chem. Soc. Rev.*, 2021, **50**, 12450–12550.
- 13 L. Wang, G.-R. Li, Q. Zhao and X.-P. Gao, *Energy Storage Mater.*, 2017, **7**, 40–47.
- 14 L. Liang, Y. Cai, X. Li, M. K. Nazeeruddin and P. Gao, *Nano Energy*, 2018, **52**, 211–238.
- 15 M. Que, B. Zhang, J. Chen, X. Yin and S. Yun, *Mater. Adv.*, 2021, **2**, 5560–5579.
- 16 K. Domanski, J. P. Correa-Baena, N. Mine, M. K. Nazeeruddin, A. Abate, M. Saliba, W. Tress, A. Hagfeldt and M. Grätzel, *ACS Nano*, 2016, **10**, 6306–6314.
- 17 N. N. Shlenskaya, N. A. Belich, M. Grätzel, E. A. Goodilin and A. B. Tarasov, *J. Mater. Chem. A*, 2018, **6**, 1780–1786.
- 18 L. Fagiolari and F. Bella, *Energy Environ. Sci.*, 2019, **12**, 3437–3472.
- 19 A. Kay and M. Grätzel, *Sol. Energy Mater. Sol. Cells*, 1996, **44**, 99–117.
- 20 D. Bogachuk, R. Tsuji, D. Martineau, S. Narbey, J. P. Herterich, L. Wagner, K. Sugiyama, S. Ito and A. Hinsch, *Carbon*, 2021, **178**, 10–18.
- 21 M. A. K. L. Dissanayake, J. M. K. W. Kumari, G. K. R. Senadeera, T. Jaseetharan, J. Weerasinghe and H. Anwar, *Mater. Sci. Eng., B*, 2021, **273**, 115440.
- 22 L. Zhang, T. Liu, L. Liu, M. Hu, Y. Yang, A. Mei and H. Han, *J. Mater. Chem. A*, 2015, **3**, 9165–9170.
- 23 A. S. A. Ahmed, W. Xiang, F. S. M. Hashem and X. Zhao, *Sol. Energy*, 2021, **230**, 902–911.
- 24 R. Cruz, J. P. Araújo, L. Andrade and A. Mendes, *J. Mater. Chem. A*, 2014, **2**, 2028–2032.
- 25 P. Mariani, A. Agresti, L. Vesce, S. Pescetelli, A. L. Palma, F. Tomarchio, P. Karagiannidis, A. C. Ferrari and A. Di Carlo, *ACS Appl. Energy Mater.*, 2021, **4**, 98–110.
- 26 C. O. Teixeira, L. Andrade and A. Mendes, *Int. J. Energy Res.*, 2019, **43**, 7541–7546.
- 27 Y. Wang, H. Zhao, Y. Mei, H. Liu, S. Wang and X. Li, *ACS Appl. Mater. Interfaces*, 2019, **11**, 916–923.
- 28 F. Yu, Y. Shi, W. Yao, S. Han and J. Ma, *J. Power Sources*, 2019, **412**, 366–373.
- 29 F. Meng, Y. Zhou, L. Gao, Y. Li, A. Liu, Y. Li, C. Zhang, M. Fan, G. Wei and T. Ma, *Mater. Today Energy*, 2021, **19**, 100590.
- 30 M. Bidikoudi, V. Dracopoulos and E. Stathatos, *Energy Adv.*, 2022, **1**, 76–86.
- 31 N. Ahn, I. Jeon, J. Yoon, E. I. Kauppinen, Y. Matsuo, S. Maruyama and M. Choi, *J. Mater. Chem. A*, 2018, **6**, 1382–1389.
- 32 M. Wu, M. Sun, H. Zhou, J.-Y. Ma and T. Ma, *Adv. Funct. Mater.*, 2020, **30**, 1906451.
- 33 D. Raptis, V. Stoichkov, S. M. P. Meroni, A. Pockett, C. A. Worsley, M. Carnie, D. A. Worsley and T. Watson, *Curr. Appl. Phys.*, 2020, **20**, 619–627.
- 34 P. Meredith and A. Armin, *Nat. Commun.*, 2018, **9**, 5261.
- 35 L. Gao, L. Chen, S. Huang, X. Li and G. Yang, *ACS Appl. Energy Mater.*, 2019, **2**, 3851–3859.
- 36 A. I. Pereira, J. Martins, C. J. Tavares, L. Andrade and A. Mendes, *Appl. Surf. Sci.*, 2017, **423**, 549–556.
- 37 B. Wilkinson, N. L. Chang, M. A. Green and A. W. Y. Ho-Baillie, *Prog. Photovoltaics Res. Appl.*, 2018, **26**, 659–674.
- 38 K. Okada, H. Matsui, T. Kawashima, T. Ezure and N. Tanabe, *J. Photochem. Photobiol., A*, 2004, **164**, 193–198.
- 39 D. Ivanou, J. Capitão, J. Maçaira, A. I. Pereira and A. Mendes, *J. Electrochem. Soc.*, 2018, **165**, H1040–H1046.
- 40 V. C. M. Duarte, D. Ivanou, G. Bernardo, L. Andrade and A. Mendes, *Int. J. Energy Res.*, 2022, **46**, 5288–5295.
- 41 A. Khan, C. Liang, Y.-T. Huang, C. Zhang, J. Cai, S.-P. Feng and W.-D. Li, *Adv. Eng. Mater.*, 2019, **21**, 1900723.
- 42 A. Khan, Y.-T. Huang, T. Miyasaka, M. Ikegami, S.-P. Feng and W.-D. Li, *ACS Appl. Mater. Interfaces*, 2017, **9**, 8083–8091.
- 43 K. Miettunen, T. Saukkonen, X. Li, C. Law, Y. K. Sheng, J. Halme, A. Tiihonen, P. R. F. Barnes, T. Ghaddar, I. Asghar, P. Lund and B. C. O'Regan, *J. Electrochem. Soc.*, 2012, **160**, H132–H137.
- 44 Z. Ku, X. Xia, H. Shen, N. H. Tiep and H. J. Fan, *Nanoscale*, 2015, **7**, 13363–13368.
- 45 H. P. Feng, T. Paudel, B. Yu, S. Chen, Z. F. Ren and G. Chen, *Adv. Mater.*, 2011, **23**, 2454–2459.
- 46 G.-R. Li and X.-P. Gao, *Adv. Mater.*, 2020, **32**, 1806478.
- 47 M. Mohammadnezhad, G. S. Selopal, N. Alsayari, R. Akilimali, F. Navarro-Pardo, Z. M. Wang, B. Stansfield, H. Zhao and F. Rosei, *J. Electrochem. Soc.*, 2018, **166**, H3065–H3073.
- 48 H. G. Lemos, D. Barba, G. S. Selopal, C. Wang, Z. M. Wang, A. Duong, F. Rosei, S. F. Santos and E. C. Venancio, *Sol. Energy*, 2020, **207**, 1202–1213.
- 49 G. A. Di Bari, *Modern Electroplating*, 2010, pp. 79–114. , DOI: [10.1002/9780470602638.ch3](https://doi.org/10.1002/9780470602638.ch3).
- 50 S. Sarker, H. W. Seo, Y.-K. Jin, M. A. Aziz and D. M. Kim, *Mater. Sci. Semicond. Process.*, 2019, **93**, 28–35.
- 51 R. B. H. Tahar, T. Ban, Y. Ohya and Y. Takahashi, *J. Appl. Phys.*, 1998, **83**, 2631–2645.
- 52 S. Ngamsinlapasathian, T. Sreethawong, Y. Suzuki and S. Yoshikawa, *Sol. Energy Mater. Sol. Cells*, 2006, **90**, 2129–2140.



- 53 S. Sheehan, P. K. Surolia, O. Byrne, S. Garner, P. Cimo, X. Li, D. P. Dowling and K. R. Thampi, *Sol. Energy Mater. Sol. Cells*, 2015, **132**, 237–244.
- 54 Q. Wei, Z. Yang, D. Yang, W. Zi, X. Ren, Y. Liu, X. Liu, J. Feng and S. Liu, *Sol. Energy*, 2016, **135**, 654–661.
- 55 A. Mei, X. Li, L. Liu, Z. Ku, T. Liu, Y. Rong, M. Xu, M. Hu, J. Chen, Y. Yang, M. Grätzel and H. Han, *Science*, 2014, **345**, 295.
- 56 D. Li, P. Jiang, W. Zhang, J. Du, C. Qiu, J. Liu, Y. Hu, Y. Rong, A. Mei and H. Han, *Solar RRL*, 2021, 2100554.
- 57 A. Verma, D. Martineau, S. Abdolhosseinzadeh, J. Heier and F. Nüesch, *Mater. Adv.*, 2020, **1**, 153–160.
- 58 A. Priyadarshi, L. J. Haur, P. Murray, D. Fu, S. Kulkarni, G. Xing, T. C. Sum, N. Mathews and S. G. Mhaisalkar, *Energy Environ. Sci.*, 2016, **9**, 3687–3692.
- 59 J. Du, C. Qiu, S. Li, W. Zhang, W. Zhang, Y. Wang, Z. Qiu, Q. Wang, K. Yang, A. Mei, Y. Rong, Y. Hu and H. Han, *Adv. Energy Mater.*, 2022, **12**, 2102229.
- 60 Y. Xia, X. Chen, Z. Zheng, X. Xiao, C. Ling, M. Xia, J. Gong, L. Gao, J. Xiang, Y. Hu, A. Mei, Y. Rong and H. Han, *J. Phys. Chem. Lett.*, 2022, **13**, 2144–2149.
- 61 K. Chen, Z. L. Zhang, J. Liu, Y. Huang, D. J. Wang, B. She, B. C. Liu, X. L. Zhang and J. Zhang, *Adv. Mater. Interfaces*, 2022, **9**, 2100395.
- 62 C. Xu, Z. Zhang, Y. Hu, Y. Sheng, P. Jiang, H. Han and J. Zhang, *J. Energy Chem.*, 2018, **27**, 764–768.
- 63 S. G. Hashmi, D. Martineau, X. Li, M. Ozkan, A. Tiihonen, M. I. Dar, T. Sarikka, S. M. Zakeeruddin, J. Paltakari, P. D. Lund and M. Grätzel, *Adv. Mater. Technol.*, 2017, **2**, 1600183.

